J. Fluid Mech. (2024), *vol*. 996, A10, doi:10.1017/jfm.2024.684

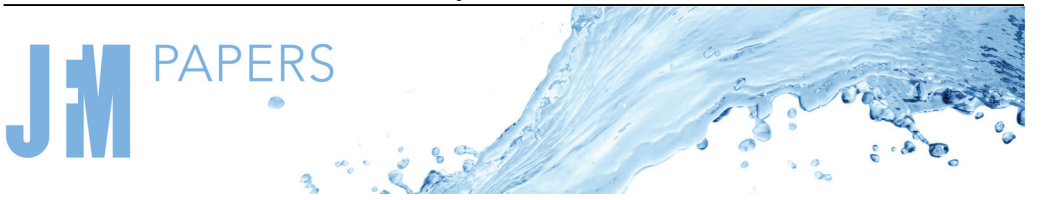

Spreading of a viscous drop after impact onto a spherical target

Mete Abbot[1], Max Lannert[1], Awadhesh Kiran[1], Shamit Bakshi[2], Jeanette Hussong[1] and Ilia V. Roisman[1],†

[1]Technische Universität Darmstadt, Institute for Fluid Mechanics and Aerodynamics, Peter-Grünberg-Straße 10, 64287 Darmstadt, Germany

[2]Department of Mechanical Engineering, IIT Madras, Chennai 600036, India

(Received 17 November 2023; revised 15 April 2024; accepted 9 June 2024)

Drop collision with a solid particle is a ubiquitous phenomenon in a wide range of applications, including rain, spray coating, cooling or cleaning, particle encapsulation, inkjet printing, and additive manufacturing. Understanding the dynamics of drop collision is essential for optimizing these processes. In this study, we present a comprehensive experimental and analytical investigation of non-axisymmetric as well as axisymmetric drop impact on a solid particle. We use a high-speed video system to visualize the drop profile during the impact, and measure the drop height and spreading diameter for different liquid viscosities, ratios of the target to drop diameters, offsets, and various other impact parameters. We then develop a theoretical model for drop spreading on a solid spherical particle that relies on the formulation of a remote asymptotic solution for the inviscid flows, generated by non-axisymmetric drop impact. Next, the viscous effects in a thin viscous boundary layer are considered, which allows the formulation of an expression for the residual lamella thickness and maximum spreading. The theoretically predicted evolution of the lamella thickness, the residual film thickness, and the maximum spreading angle agree well with the experimental data presented in this work and the literature. Finally, we present a novel approach for *in situ* measurement of liquid viscosity, drop impact viscometry, at high shear rates via a single drop impact experiment, with potential application in industries where non-Newtonian drops play a major role, such as pesticide spraying, paint droplet spreading, blood drop impact and fuel injectors.

Key words: drops, Navier–Stokes equations

† Email address for correspondence: roisman@sla.tu-darmstadt.de

1. Introduction

The flow induced by drop impact is governed by different forces, such as inertial, viscous, capillary and interfacial forces associated with the wettability of the substrate. The study initiated by Worthington (1876) more than 130 years ago has been intensified recently by new opportunities related to the emergence of high-resolution and high-speed digital video systems allowing detailed observation and measurement of the drop impact process. The fluid dynamic phenomenon of liquid drop impact has become an essential research area of fluid mechanics that has been studied extensively in the last century (Yarin 2006; Marengo *et al.* 2011; Josserand & Thoroddsen 2016; Yarin, Roisman & Tropea 2017). The studies are motivated by various industrial applications wherever spray or droplet deposition is part of the process, including but not limited to printing, three-dimensional printing, spray coating, spray cooling, fuel injection, fire suppression sprinkling and medical drops. Systematic studies of drop impact under various conditions are already present in the literature, such as drop impact on solid flat surfaces (Rioboo, Marengo & Tropea 2002; Cheng, Sun & Gordillo 2022) or curved surfaces (Bakshi, Roisman & Tropea 2007; Mitra *et al.* 2017; Luo *et al.* 2021; Sykes *et al.* 2022), onto substrates wetted by a thin liquid film (Yarin & Weiss 1995; Cossali, Coghe & Marengo 1997; Kittel, Roisman & Tropea 2018) or into deep liquid pools (Bisighini *et al.* 2010; Fudge *et al.* 2023). More complex interactions of drops with surfaces include impact onto another drop (Jaiswal & Khandekar 2021) or bubble (Zhang *et al.* 2022), onto soft surfaces (Howland *et al.* 2016) or surfaces of complex morphology (Mock *et al.* 2005; Lembach *et al.* 2010; Roisman, Lembach & Tropea 2015).

The impact outcomes in the isothermal case (Rioboo, Tropea & Marengo 2001) include drop deposition, drop corona splash, prompt splash and drop rebound. This is determined by the initial drop size, impact velocity, surface tension, viscosity, surface properties (such as surface morphology and the wetting properties), and the physical and molecular densities of the surrounding gas (Riboux & Gordillo 2014). These outcomes are mapped as a function of Weber number, Reynolds number and Froude number,

$$We = \rho U_0^2 D_0/\sigma, \quad Re = \rho U_0 D_0/\mu, \quad Fr = U_0^2/gD_0, \tag{1.1a–c}$$

where ρ, σ, μ, D_0 and U_0 are the density, surface tension, viscosity, initial diameter and initial velocity before impact, respectively, while g is the gravitational acceleration ($9.81\ \mathrm{m\ s^{-2}}$).

Drop impact onto a flat substrate can be subdivided into several main stages: (i) initial drop deformation; (ii) fast radial spreading characterized by the creation of a thin lamella, bounded by a rim; (iii) reaching the maximum spreading; and then, if the surface is hydrophobic, (iv) rim receding.

The inertia-dominated flow in the spreading lamella can be well approximated by the remote asymptotic solution for an inviscid flow obtained by Yarin & Weiss (1995). This solution is valid at times when the lamella thickness is higher than the thickness of the viscous boundary layer developed immediately after the drop impact. The self-similar analytical solution for the flow in the boundary layer corresponding to the inviscid, asymptotic, radial flow in the film has been obtained in Roisman (2009). The thickness of this boundary layer can be estimated as $h_v \sim \sqrt{\nu t}$.

Finally, when the film thickness becomes comparable with the thickness of the boundary layer, the viscosity effects are significant. These effects lead to the flow deceleration and formation of the residual stationary liquid film. The thickness of the residual film in the case of drop impact onto a dry flat substrate is predicted in Roisman (2009) in the form $h_{res} \approx 0.79 D_0\, Re^{-2/5}$. This scaling has also been confirmed for the case of drop impact onto a liquid film (Berberović *et al.* 2009; Stumpf, Hussong & Roisman 2022).

Furthermore, through experimenting with drop impact on a spherical target, Bakshi *et al.* (2007) identified three different temporal phases of the film dynamics, namely the initial drop deformation phase, the inertia-dominated phase, and the viscosity-dominated phase. The thickness of the spreading liquid in the first two phases is independent of both the liquid properties and the surface properties, while in the viscous phase, the thickness is governed solely by the liquid viscosity. The advantage of the spherical target is that a clear view of the lamella was obtained without it being obscured by the rims. Consequent numerical and experimental studies have shown similar results (Zhang, Papadikis & Gu 2014; Zhu *et al.* 2017). Slight deviations were reported at low Reynolds numbers in the viscosity-dominated regime, which were related to the wettability of the surface (Mitra *et al.* 2017). Other studies (Mitra *et al.* 2016; Liu, Zhang & Min 2019; Dalgamoni & Yong 2021; Fan *et al.* 2023) used energy balance and mass conservation to correlate the droplet residual height with the maximum spreading angle and the spherical target diameter.

Apart from droplet height, the maximum spreading of a drop is one of the major criteria that control the quality of inkjet printing, spray coating, and even medical drop applications such as eye drops. Extensive studies have been devoted to estimating the maximum spreading, represented by the maximum spreading factor D^*_{max}, experimentally, numerically and theoretically. Some of the earliest studies described D^*_{max} in a semi-empirical model in the form $D^*_{max} = a(Re\sqrt{We})^b$ (Scheller & Bousfield 1995; Marmanis & Thoroddsen 1996). Several consequent experimental studies did not agree completely with the initial prediction, leading to several other semi-empirical functions, and consequently to the well-known analytical self-similar solution for the viscous flow in the spreading drop that satisfies the full Navier–Stokes equations introduced by Roisman (2009) using experimental data from Roisman, Rioboo & Tropea (2002), Pasandideh-Fard *et al.* (1996), Cheng (1977) and Scheller & Bousfield (1995):

$$D^*_{max} \approx 0.87\, Re^{1/5} - 0.40\, Re^{2/5}\, We^{-1/2}. \tag{1.2}$$

Similar empirical models have been proposed later on and are summarized in Aksoy *et al.* (2022), while most recently, Tang *et al.* (2017) accounted for roughness. Nonetheless, these models typically overlook the influence of substrate wettability and roughness. The energy balance method is often employed to model D^*_{max}, especially when the details of the flow are not known but the substrate wettability is known, effectively modelling the kinetic energy, surface energy and viscous dissipation. Pasandideh-Fard *et al.* (1996) computed D^*_{max} as a function of advancing contact angle, *We* and *Re*, while Ukiwe & Kwok (2005) proposed using energy balance to predict D^*_{max} as the root of a dimensionless cubic equation:

$$(We + 12)D^*_{max} = 8 + D^{*3}_{max}[3(1 - \cos\theta) + 4\, We\, Re^{-1/2}]. \tag{1.3}$$

Refinements of the energy-balance-based estimations are still being researched to date, while the improvements in the agreement with the experimental data are already satisfactory (Mao, Kuhn & Tran 1997; Gao & Li 2014; Wildeman *et al.* 2016; Du *et al.* 2021). Some studies used similar modelling to predict the maximum spreading on a spherical target (Khurana, Sahoo & Dhar 2019). Experimental and numerical studies show that higher Weber numbers and smaller particle sizes increases the droplet's maximum spreading coefficient (Yan-Peng & Huan-Ran 2011), while a reduced contact angle increases the particle's maximum spreading area (Liu *et al.* 2019; Fan *et al.* 2023). Recently, Yoon & Shin (2021) provided several empirical correlations for various viscosities and target curvatures at low-impact energy. It is worth noting that most of these studies are performed with low impact velocity, while higher impact velocities

are more likely to be less affected by surface wettability. The effect of wettability on maximum spreading for targets that are smaller than the droplets has been studied both experimentally (Banitabaei & Amirfazli 2017) and numerically (Dalgamoni & Yong 2021). Studies on the collision of drops with a moving spherical particle revealed how the motion of the target could highly influence the drop impact's outcome (Mitra *et al.* 2013; Sechenyh & Amirfazli 2016; Banitabaei & Amirfazli 2020).

At some impact and geometrical conditions, drop impact may lead to the lamella detachment and splash. Hardalupas, Taylor & Wilkins (1999) carried out an experimental investigation of sub-millimetre droplet impingement onto the spherical surface, where the target diameter is of the order of 1 mm, finding that increasing surface curvature promoted the onset of atomization, while the splash crown shape was influenced by surface morphology. This study initiated a recent series of experimental and theoretical studies on small spherical targets (0.4 mm $> D_s >$ 2mm) with even smaller drop sizes (100 μm $> D_s >$ 500 μm). Charalampous & Hardalupas (2017) discovered an intermediate regime, near the splash onset, where the droplet forms a stable crown that does not break up but propagates along the particle surface and passes around the particle, highlighting the possibility of complete particle coating by drop impact. Pawar *et al.* (2016), Mitra *et al.* (2017) and Bordbar *et al.* (2018) studied slightly larger droplets with equivalent target sizes at low capillary numbers, and developed regime maps to differentiate between merging and breaking cases. Sykes *et al.* (2022) revealed that the splashing phenomenon can be mitigated through substrate curvature. Importantly, this effect persists regardless of whether the substrate is convex or concave, implying that smaller spheres inherently offer increased resistance to droplet splashing.

This study is focused on the development of a solution for a basic fluid flow associated with the non-axisymmetric spreading of a drop on a solid spherical surface. This solution, valid for inertia-dominated drop impacts, allows us to predict the evolution of the drop shape, the distribution of the thickness of the residual film, and the spreading factor of the drop. Finally, we demonstrate how such a set-up could be used to measure viscosity, resulting in a novel viscosity measurement technique that is accurate, fast, and requires only a single droplet in the range of microlitres.

2. Experimental method

2.1. *Experimental set-up*

A schematic of the experimental set-up used in this study is shown in figure 1(*a*). It consists of a syringe pump, a vertical stage, a stainless steel spherical target, and two perpendicularly mounted high-speed CMOS cameras, all mounted on a passive pneumatic vibration isolation table. An AL 300 Aladdin InfusionONE Syringe (World Precision Instruments Germany GmbH, Germany) is set to flow rate 0.3 ml min^{-1}, with a blunt bevel facet 21G needle with external diameter 0.8 mm allowing the generation of drops with consistent size, 2.2–3 mm diameter. The size of the drop is determined by the balance of surface tension and the weight of the drop. Impact velocities are determined by changing the vertical impact distance between the needle tip and the apex of the sphere. The height and position are adjusted using a millimetre-precise stepper motor vertical stage, followed by finer adjustment with an XYZ-microstage. In this way, velocities up to 4.5 m s^{-1} are achieved. A protective acrylic tube helps to stabilize the trajectory of the drop.

Mirror-polished stainless steel (AISI 304) spherical targets with diameters 6, 30, 40 and 50 mm are used. The roughness is $R_a = 0.15 \pm 0.05$ μm as reported by the manufacturer. The static contact angle for an equivalent flat AISI 304 surface is $85 \pm 5^\circ$. Contact angle

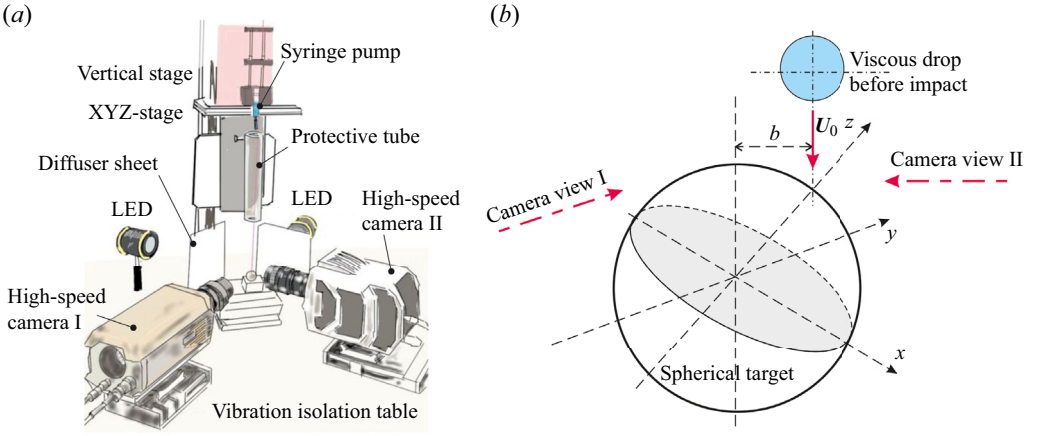

Figure 1. Experimental set-up: (*a*) sketch of the main systems of the set-up, and (*b*) schematic view of the spherical target and impacting drop.

hysteresis is known to be small for this type of material (AISI304), at $\approx 7^\circ$ (Pou *et al.* 2019). The spheres are cleaned with acetone, isopropanol and distilled water, and dried before every experiment. Two CMOS high-speed cameras (Vision Research Inc., Germany) were utilized to image the impact from two perpendicular angles. A Phantom v12 with resolution 1024 × 512 pixels, combined with a macro lens to obtain a wider view (pixel size 25 μm pixel^{-1}), captured the impact and spreading of the drop at 10 000 frames per second (fps). A Phantom v2012 with resolution 1280 × 800 pixels, combined with a ×5 zoom macro lens to obtain a higher spatial resolution (pixel size 4 μm), is used to measure the thickness of the lamella at 10 000 fps. Both cameras measured the offset of the drop from the centre of the target to ensure that the drop impact was exactly at the centre of the spherical target. Both cameras have an image-based auto-trigger that engages when the drop arrives in the proximity of the target. In order to achieve shadowgraphy high-speed imaging, backlighting Constellation 120E LED illumination (Imaging Solution GmbH, Germany) is placed behind the drop. A diffuser sheet with diffusion angle 80° is placed between the LED illumination and the impact zone of the drop in order to achieve more uniform illumination of the falling drop. A Brookfield DV-III Ultra programmable rheometer (AMETEK GmbH, Germany) equipped with cone/plate is used to measure the viscosities of all the samples, using 0.5 ml sample size with adequate modes, plate type and frequency modulation based on the manufacturer's recommendations. Surface tension is measured using a Tensíío force tensiometer (KRÜSS GmbH, Germany) with the recommended settings by the manufacturer for the Wilhelmy plate method. The error for viscosity measurements in table 1 is below 1 % in all the samples. The repeatability of the surface tension measurement is below 0.2 mN m^{-1} for all samples.

The drops used in all experiments are made of $\geqslant$99.5 % anhydrous glycerol (Carl Roth GmbH, Germany) and distilled water aqueous solutions with varying volume fractions. Prior to performing the experiments, the critical properties of the liquids are measured. Table 1 presents an overview of the liquids used in the experiments, and their physical properties. For brevity, the samples will be referred to as H2O for distilled water, and Gly40, Gly60, Gly80, Gly90, Gly95 and Gly100 for glycerol solutions of corresponding percentage.

Fluid	Density (kg m^{-3})	Viscosity (mPa s)	Surface tension (mN m^{-1})
Distilled water	998.1	1	72.3
40 % glycerol solution	1103.2	5	67.6
60 % glycerol solution	1155.7	16.3	66.5
80 % glycerol solution	1208.3	90.2	66.3
90 % glycerol solution	1234.5	302	65.7
95 % glycerol solution	1247.7	632.4	65.4
Glycerol	1260.8	1421	63.4
Isopropanol	785.0	2.1	21.2

Table 1. Properties of liquids at temperature $T = 20\,^{\circ}$C used in this work.

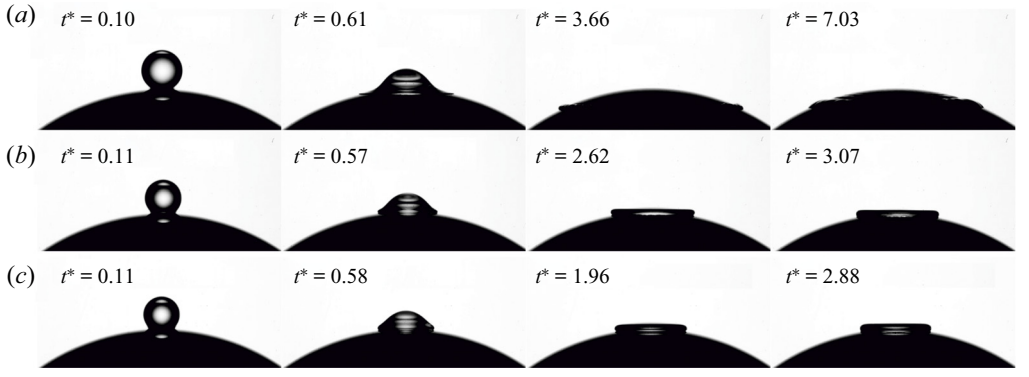

Figure 2. Axisymmetric impact of (*a*) water, (*b*) Gly80 and (*c*) Gly90 drops. The impact velocity is $U_0 = 3$ m s^{-1}, $10 < D_s/D_0 < 11.4$, and the target diameter is $D_s = 30$ mm. The frames correspond to the initial drop deformation, end of the phase of inertial spreading, instant of minimum lamella thickness, and instant of maximum spreading diameter, respectively.

In this study, the drop spreading factor and the evolution of the lamella thickness are measured for the spherical targets of diameters from the moment of impact until times well beyond the maximum spreading. The impact velocities are between 1 and 4 ms^{-1}, while drop diameters were in the range 2.2–3 mm. The reason for the variation in drop size is that liquids also varied in surface tension.

2.2. *Observations of axisymmetric and non-axisymmetric drop spreading*

Exemplary images of the liquid film profile acquired at different instants after impact are shown in figures 2 and 3 for axisymmetric and non-axisymmetric impacts, respectively. The impact parameters of the experiments shown in these figures correspond to Reynolds number $Re = 5200$ and Weber number $We = 142$. The off-axis distance for figure 3 is 1.12 mm.

For larger off-axis distances as shown in figure 3, the droplet grazes on the edge of the target and leaves behind a small coated part on the target surface. The larger part of the liquid mass continues to move as a smaller droplet. The smaller droplets impacting onto a larger target spread, recede, and then remain deposited on the surface.

The main stages of drop collision with a spherical target and the geometrical parameters used in the further analysis are shown in figure 4, as observed from the high-speed video

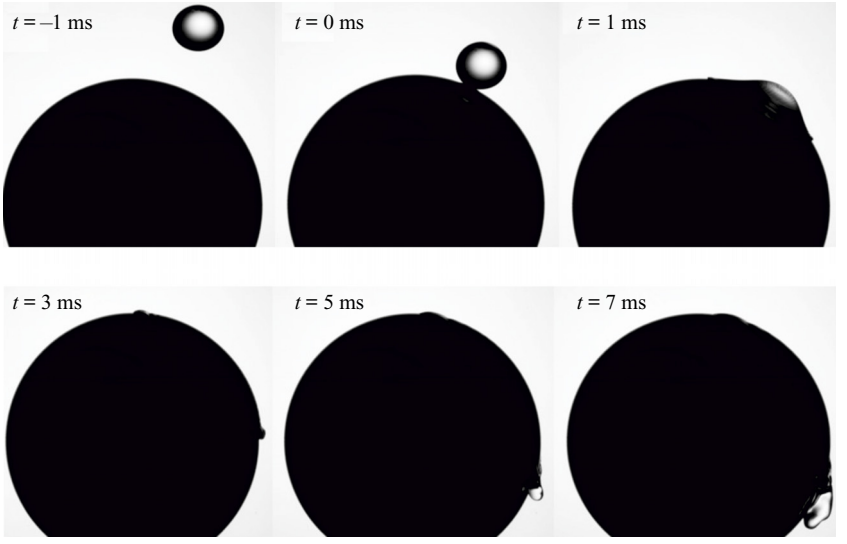

Figure 3. Non-axisymmetric impact of a water drop. The impact parameters are: initial drop diameter $D_0 = 3$ mm, impact velocity $U_0 = 2$ m s^{-1}, off-axis distance $b = 3.76$ mm, target diameter $D_s = 15$ mm.

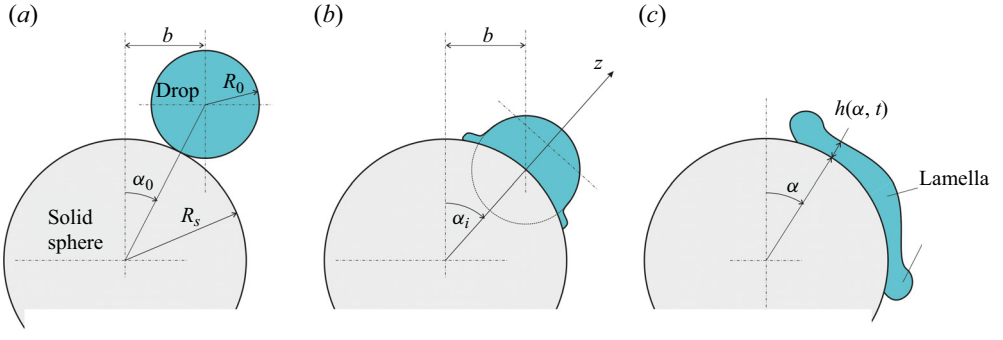

Figure 4. Sketch of non-axisymmetric drop impact and its initial deformation: (*a*) instant of impact when drop touches the sphere ($t = 0$); (*b*) typical drop deformation at $t = t_i$, at which the virtual centre of the drop arrives on the target's surface; (*c*) spreading of a drop lamella, $t \gg t_i$.

system I. The initial radius of the drop is given as $R_0 = D_0/2$, and that of the rigid spherical target as $R_s = D_s/2$. The impact velocity is denoted as U_0, and the off-axis distance is denoted as b (see figure 4*a*). Let us indicate the intersection point of the impact axis with the target surface as the impact point. Its position at the spherical surface of the target can be defined by angle $\alpha_i = \arcsin[b/R_s]$ with the vertical axis. The typical velocity parallel to the target surface U_τ can be estimated from the geometrical considerations $U_\tau = U_0 b/R_s = U_0 \sin\alpha_i$. The corresponding normal velocity component is defined as $U_n = U_0 \cos\alpha_i$.

The instant $t = 0$ is the first instant when the drop touches the target (figure 4*a*). The position of the point at the target's surface where the drop first touches the target is determined by the angle $\alpha_0 \equiv \arcsin[b/(R_s + R_0)]$. At $t > 0$, a drop starts to deform and spread. The instant corresponding to the case shown in figure 4(*b*) can be estimated as $t_i = R_0 \cos\alpha_0/U_0$. The drop spreading in a thin lamella is observed at times $t \gg t_i$.

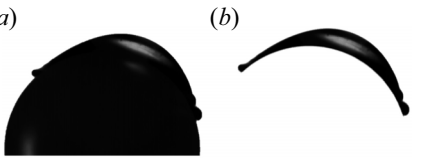

Figure 5. Image of the film produced by drop impact: (*a*) the original image; (*b*) the image of a film profile obtained by subtracting the dry target.

2.3. *Image processing and post-processing*

A Matlab code has been developed to perform the image processing and post-processing of the videos obtained from the cameras. First, the code converts the images obtained from each camera into binary images. Then, to detect the drop, the target and the background, it sorts all the detected objects in each image based on their roundness. Consequently, any disturbance aside from the drop and the target are filtered out, and the diameter and velocity of the drop right before impact is then measured. The equivalent diameter of a disc with an equal area method is used in all the calculations, i.e. diameter $= 2 \times \text{area}/\pi$. Both the vertical diameter and horizontal diameter are measured for every experiment. The difference was not significant in any of the experiments. Additionally, drop oscillations are dampened by the liquid viscosity, especially at higher velocities. To guarantee the alignment of the impact, the code identifies the centre of the drop and the apex of the target, and measures their corresponding offset. Finally, the code subtracts the spherical target from the images to measure the thickness of the lamella and the spreading diameter throughout the experiment using the videos from the Phantom v2012 and Phantom v12 cameras, respectively. Demonstration of the target subtraction is shown in figure 5.

The cases with an overall offset of less than 1 % with respect to the target are considered axisymmetric. For the offset experiments, the two cameras are used simultaneously to make sure that the offset is in only one direction, while the other is centred within 1 % with respect to the target. This guarantees that the drop will not fall behind or in front of the contact line in the plane of the view of the camera observing the offset.

3. Inviscid flow in a thin film on a sphere

3.1. *Remote asymptotic solution*

Consider a flow generated by a single drop impact. If the Reynolds and Weber numbers are high enough, then the flow in the lamella is governed mainly by the inertia, if the lamella is much thicker than the viscous boundary layer. Therefore, we start now with the solution for the inviscid flow in a thin liquid film on a spherical surface.

The flow dynamics in a thin drop lamella is described in a spherical coordinate system $\{r, \theta, \varphi\}$ with the origin at the sphere centre, where r is the radial coordinate, θ is the polar angle, and φ is the azimuthal angle. Denote as u_θ the average through the lamella cross-section velocity component of the liquid in the θ-direction, and u_φ in the φ-direction. A sketch of the spherical coordinate system and the corresponding spherical coordinates of an arbitrary point r on the sphere surface is presented in figure 6. In a thin film, the radial component of the velocity, normal to the substrate, is much smaller than u_θ. We consider only the impact with high Weber, Froude and Reynolds numbers, for which the effects of surface tension, gravity and viscosity are minor in comparison with the inertia. The momentum balance equations for the flow in the thin lamella whose thickness $h(\theta, t)$

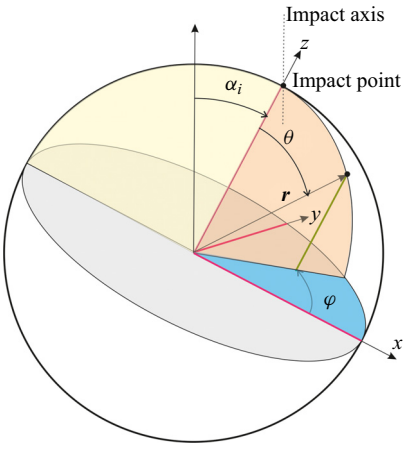

Figure 6. Sketch of the spherical coordinate system and the corresponding spherical coordinates of an arbitrary point $\boldsymbol{r}$ on the sphere surface.

is much smaller than R_s are reduced to

$$\frac{1}{\rho}\frac{\partial p}{\partial r} = \frac{u_\theta^2 + u_\varphi^2}{R_s}, \tag{3.1}$$

$$\frac{1}{\rho}\frac{\partial p}{\partial \theta} = R_s\frac{\partial u_\theta}{\partial t} + u_\theta\frac{\partial u_\theta}{\partial \theta} + \frac{u_\varphi}{\sin\theta}\frac{\partial u_\theta}{\partial \varphi} - u_\varphi^2\cot\theta, \tag{3.2}$$

$$\frac{1}{\rho\sin\theta}\frac{\partial p}{\partial \varphi} = R_s\frac{\partial u_\varphi}{\partial t} + u_\theta\frac{\partial u_\varphi}{\partial \theta} + \frac{u_\varphi}{\sin\theta}\frac{\partial u_\varphi}{\partial \varphi} + u_\theta u_\varphi\cot\theta. \tag{3.3}$$

The pressure in the lamella, estimated from (3.1), is $p \sim \rho h u^2/R_s$, where h is the lamella thickness, and $u \equiv u_\theta^2 + u_\varphi^2$. The pressure gradient along the trajectory of an arbitrary material point, moving with the flow, is

$$\frac{\partial p}{\partial s} \sim \rho u\frac{\partial u}{\partial s}\frac{h}{R_s} \ll \rho u\frac{\partial u}{\partial s}, \tag{3.4}$$

where s is the path measured along the particle trajectory. The pressure gradients are thus negligibly small in comparison with the inertial effects. An arbitrary material point in the lamella flows along a geodesic line with a constant absolute velocity. It is known that the geodesic lines on a sphere are the great circles.

Consider an arbitrary material point, initially located at $\boldsymbol{r}_0 = \{\theta_0, \varphi_0\}$. The corresponding components of the initial velocity $\boldsymbol{u}_0(\theta_0, \varphi_0)$ of this point are denoted $u_{\theta 0}$ and $u_{\varphi 0}$. The radius vector of this point at $t > 0$ is denoted $\boldsymbol{r}(t)$. The unit vector $\boldsymbol{n}$ normal to the great circle along which the considered point moves is

$$\boldsymbol{n} = \frac{\boldsymbol{r}_0 \times \boldsymbol{u_0}}{R_s u_0}, \quad u_0 = \sqrt{u_{\theta 0}^2 + u_{\varphi 0}^2}. \tag{3.5a,b}$$

Now, the trajectory of the material point, corresponding to the initial position $\{\theta_0, \varphi_0\}$, is determined through

$$\boldsymbol{r}(t) = \boldsymbol{r}_0\cos\omega t + \boldsymbol{n}\times\boldsymbol{r}_0\sin\omega t, \quad \omega = \frac{u_0}{R_s}, \tag{3.6a,b}$$

and its velocity vector is

$$\boldsymbol{u} = u_0 \frac{\boldsymbol{n} \times \boldsymbol{r}}{R_s}. \tag{3.7}$$

The expressions for the coordinates $\theta(t)$ and $\varphi(t)$ of the material point can be derived from (3.5*a*,*b*):

$$\theta = \arccos\left[\cos\theta_0 \cos\omega t - \frac{u_{\theta 0} \sin\theta_0}{u_0} \sin\omega t\right], \tag{3.8}$$

$$\varphi = \arctan\left[\frac{u_0 \sin\varphi_0 \sin\theta_0 \cos\omega t + (u_{\varphi 0} \cos\varphi_0 + u_{\theta 0} \cos\theta_0 \sin\varphi_0) \sin\omega t}{u_0 \cos\varphi_0 \sin\theta_0 \cos\omega t - (u_{\varphi 0} \sin\varphi_0 - u_{\theta 0} \cos\theta_0 \cos\varphi_0) \sin\omega t}\right]. \tag{3.9}$$

The evolution of the lamella thickness can be expressed using the mass balance of the flow. An infinitesimal volume ΔW of an element of the lamella is determined in the form

$$\Delta W = h \left|\frac{\partial \boldsymbol{r}}{\partial\theta_0} \times \frac{\partial \boldsymbol{r}}{\partial\varphi_0}\right| \Delta\theta_0\, \Delta\varphi_0 = h_0 \left|\frac{\partial \boldsymbol{r}_0}{\partial\theta_0} \times \frac{\partial \boldsymbol{r}_0}{\partial\varphi_0}\right| \Delta\theta_0\, \Delta\varphi_0, \tag{3.10}$$

therefore

$$h = h_0(\theta_0, \varphi_0) \frac{R_s^2 \sin\theta_0}{\left|\dfrac{\partial \boldsymbol{r}}{\partial\theta_0} \times \dfrac{\partial \boldsymbol{r}}{\partial\varphi_0}\right|}. \tag{3.11}$$

In spherical coordinates, this expression yields

$$h = h_0(\theta_0, \varphi_0) \left|\frac{\sin\theta_0}{\sin\theta}\right| \left|\frac{\partial\theta}{\partial\theta_0}\frac{\partial\varphi}{\partial\varphi_0} - \frac{\partial\theta}{\partial\varphi_0}\frac{\partial\varphi}{\partial\theta_0}\right|^{-1}. \tag{3.12}$$

3.2. *Kinematics of the drop profile at the symmetry plane*

Let us take the z-axis to connect the sphere centre and the point of the drop impact. The initial distribution of the flow at $t = 0$ consists of the axisymmetric part, determined by the normal component of the impact velocity U_n, and the transverse flow, determined by the tangential component U_τ. At a point $\{\theta_0, \varphi_0\}$ on the sphere surface in the vicinity of the impact point, $\theta_0 \ll 1$, the flow can be linearized, leading to

$$u_{\theta 0} = U_n \kappa \theta_0 + U_\tau \cos\varphi_0, \quad u_{\varphi 0} = -U_\tau \sin\varphi_0, \tag{3.13a,b}$$

where κ is an unknown dimensionless constant. Consider the flow near the symmetry plane $\varphi_0 \to 0$ and $\varphi_0 \to \pi$. The linearized solution yields

$$\theta(t) = \theta_0 + \Omega t, \tag{3.14}$$

$$\varphi(t) = \left[1 - \frac{U_\tau \sin\Omega t}{u_{\theta 0} \sin(\theta_0 + \Omega t)}\right] \varphi_0, \quad \varphi \to 0, \tag{3.15}$$

$$\varphi(t) = \left[1 + \frac{U_\tau \sin\Omega t}{u_{\theta 0} \sin(\theta_0 + \Omega t)}\right] (\varphi_0 - \pi), \quad \varphi \to \pi, \tag{3.16}$$

$$\Omega = \frac{U_n \kappa \theta_0 + U_\tau \cos\varphi_0}{R_s}. \tag{3.17}$$

Expressions (3.14) and (3.17) allow us to derive the expression for the velocity in the lamella in the Eulerian form

$$u_\theta = \frac{R_s(\theta + \Delta\theta)}{t + \Delta t}, \quad \Delta t = \frac{R_s}{\kappa U_n}, \quad \Delta\theta = \frac{\Delta t\, U_\tau}{R_s}\cos\varphi_0, \tag{3.18a–c}$$

where Δt and $\Delta\theta$ are constants determined by the ratio $k = R_s/R_0$.

The expression for the lamella profile at the symmetry plane is then obtained in the form

$$h = h_0(\theta_0, \varphi_0)\left|\frac{\sin\theta_0}{\sin\theta}\right|\left|\left(1 + \frac{\kappa t U_n}{R_s}\right)\left[1 - \frac{U_\tau\cos\varphi_0\sin\Omega t}{u_{\theta 0}\sin\theta}\right]\right|^{-1}. \tag{3.19}$$

The remote asymptotic solution for the evolution of the lamella profile on the sphere is obtained, assuming $\theta_0 \ll 1$. Linearization yields

$$h = h_0(\theta_0, \varphi_0)\,\frac{\theta_0}{|\sin\theta|}\,\frac{\Delta t}{t + \Delta t}\left|1 - \frac{\Delta\theta}{\Delta t}\,\frac{R_s\sin\Omega t}{u_{\theta 0}\sin\theta}\right|^{-1}. \tag{3.20}$$

This equation is written in the dimensionless form

$$h^* = h_0^*(\theta_0, \varphi_0)\,\frac{\theta_0}{|\sin\theta|}\,\frac{\tau}{t^* + \tau}\left|1 - \frac{\chi\,\sin(\Omega^* t^*)}{\Omega^*\sin\theta}\right|^{-1}, \tag{3.21}$$

$$\Omega^* = \frac{\theta_0}{\tau} + \chi, \tag{3.22}$$

$$\chi = \frac{2\cos\varphi_0}{k}\tan\alpha_i, \quad \cos\varphi_0 = \pm 1, \tag{3.23a,b}$$

$$\theta(t^*) = \theta_0 + \Omega^* t^*, \quad \alpha = \alpha_i + \theta\cos\varphi_0, \tag{3.24a,b}$$

where $\tau = \Delta t\, U_n/D_0$ is a dimensionless constant. The shape $h^*(\alpha)$ is represented in the parametric form (3.21) with a small positive value θ_0 serving as a parameter.

3.3. *Experimental characterization of the drop profile on a spherical surface*

In order to characterize the evolution of the drop height in time, we measure only the drop height h_i at the position corresponding to $\alpha = \alpha_i$ at the impact axis; h_i is measured normal to the sphere surface along the z-axis, as shown in figure 4. In figures 7(*a*) and 7(*b*), the measurements are shown in the dimensionless form, using the drop diameter as the length scale, and the characteristic normal component of the velocity $U_n = U_0\cos\alpha_i$ as the velocity scale. Correspondingly, D_0/U_n is used as the time scale. At short times ($t^* < 10$), it is obvious that the evolution of the drop height depends weakly on α_i if these angles are relatively small, $\alpha_i < 20^\circ$. The dependence becomes more significant for higher values of α_i, shown in figure 7(*b*). The height h initially reduces in time, but at some instant reaches a plateau value, the residual thickness. The residual liquid film appears as a result of the flow-damping by viscosity when the thickness of the boundary layer is comparable with the lamella thickness. This problem has been solved for the case of normal (Roisman 2009) and oblique (Roisman 2010) impact onto a flat substrate. It is remarkable that the thickness of the residual film at $\alpha = \alpha_i$ almost does not depend on the impact inclination. This is an important practical result that can allow for improving the modelling of the particle encapsulation by drop impact.

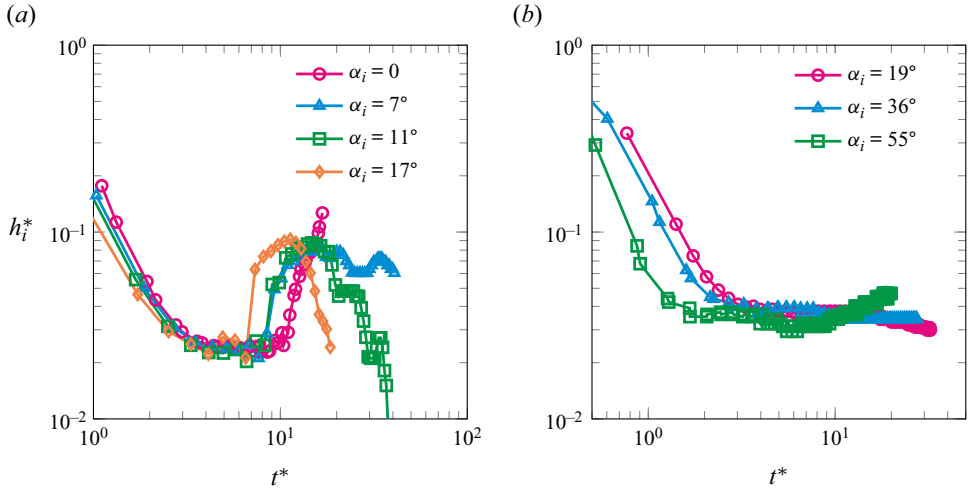

Figure 7. (*a*) Water drop impact at various off-axis lengths at the longer times after impact. The dimensionless thickness $h_i^* = h_i/D_0$ of the liquid film at the impact point $\alpha = \alpha_i$ is a function of the dimensionless time $t^* = tU_0 \cos\alpha_i/D_0$. The impact parameters are $D_0 = 2.6$ mm, $U_0 = 2.0$ m s^{-1}, $Re = 5200$, $We = 142$, and the target diameter is 6 mm. (*b*) Isopropanol drop impact at various off-axis lengths at the early stages of spreading. The dimensionless thickness $h_i^* = h_i/D_0$ of the liquid film at the impact point $\alpha = \alpha_i$ is a function of the dimensionless time $t^* = tU_0 \cos\alpha_i/D_0$. The impact parameters are $D_0 = 2.2$ mm, $U_0 = 1.37$ m s^{-1}, $Re = 985$, $We = 154$, and the target diameter is $D_s = 6$ mm.

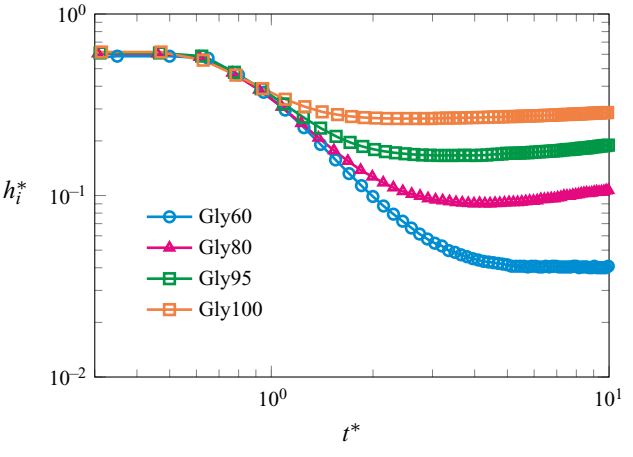

Figure 8. Effect of the liquid viscosity on the evolution of the drop height for an axisymmetric drop impact. The dimensionless thickness $h_i^* = h_i/D_0$ of the liquid film at the impact point $\alpha = 0$ is a function of the dimensionless time $t^* = tU_0/D_0$. The impact parameters are $D_0 = 2.66 \pm 0.06$ mm, $U_0 = 4$ m s^{-1}, and the target diameter is $D_s = 40$ mm.

The effect of viscosity on the evolution of the film thickness is shown in figure 8. As expected, the value of the residual film thickness increases with the liquid viscosity.

The influence of the impact angle α_i in the drop shape at the same time instant is shown in figure 9. The position of the peak of the curve, $h^*(\theta, t)$, propagates in time along the spherical surface. The average velocity of propagation of the position of the peak is compared with our estimation $U_\tau \approx U_0 \sin\alpha_i$ in figure 10. The agreement is rather good

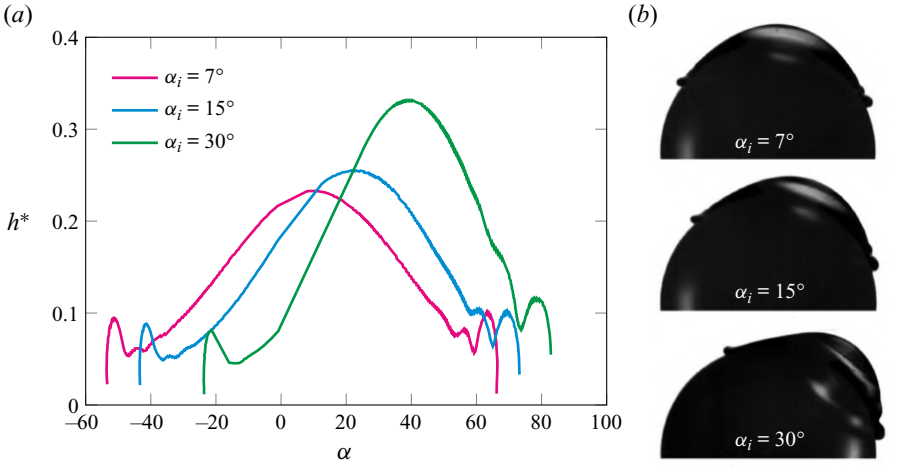

Figure 9. Distilled water drop impact. The dimensionless thickness of the liquid film is a function of the zenith angle θ for various impact angles at $t = 1.2$ ms ($tU_0/D_0 = 0.92$). The impact parameters are $D_0 = 2.6$ mm, $U_0 = 2.0$ m s^{-1}, $Re = 5200$, $We = 142$, and the target diameter is $D_s = 6$ mm.

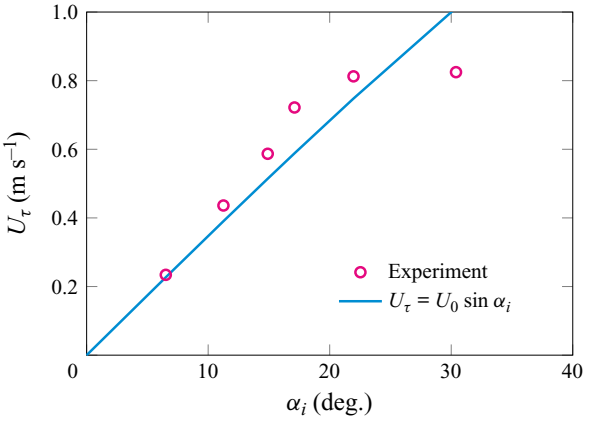

Figure 10. Tangential film velocity. Comparison of the average velocity of the film propagation with the estimated magnitude $U_0 \sin\theta_i$ at various impact angles. The impact parameters are $D_0 = 2.6$ mm, $U_0 = 2.0$ m s^{-1}, $Re = 5200$, $We = 142$, and the target diameter is $D_s = 6$ mm.

for angles $\alpha_i < 20°$. This result can be used as a justification of the assumed initial velocity distribution (3.13*a*,*b*) in the impacting drop.

The shape of the drop has been captured using the camera settings that provide a spatial resolution $\Delta x = 5$–9 μm. The possible error δ_{peak} of the estimation of the peak position depends on its curvature. In our case, it is $\delta_{peak} \approx \sqrt{D_0\,\Delta x} = 1.6 \times 10^{-4}$ m. The velocity is estimated on the time interval $\Delta t = 1$ ms. Therefore, the estimated error of the velocity estimation is $\Delta x/\Delta t = 0.16$ m s^{-1}.

Finally, the theoretical predictions (3.21) for the shape of the spreading drop are compared with the experimental data in figure 11 for impact angles $\alpha_i = 6.5°$ and $22°$. As an initial distribution of the drop height, the result from Roisman, Berberović & Tropea (2009), developed for an impact onto a flat target from the mass balance equation, is

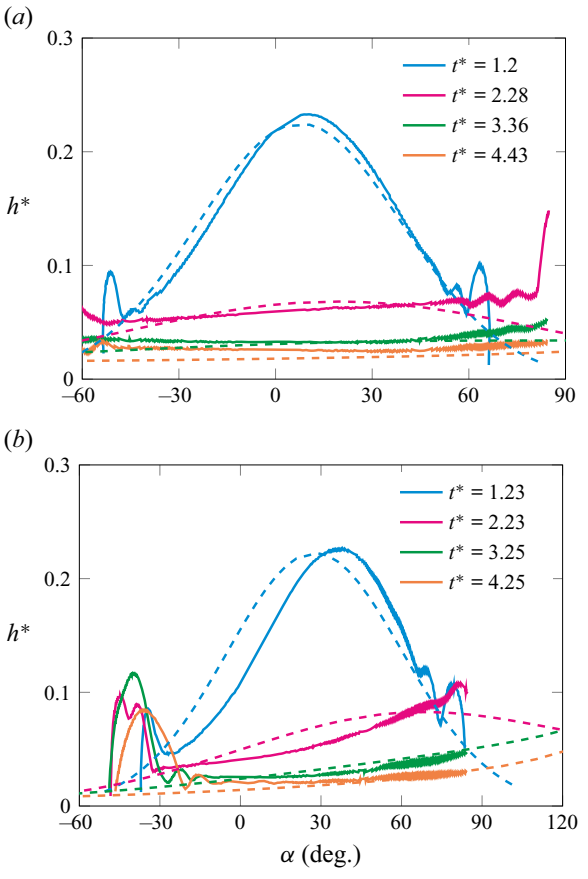

Figure 11. Measured shape of the drop profile $h^*(\alpha)$ in comparison with the theoretical predictions (dashed lines). The impact parameters are $D_0 = 2.6$ mm, $U_0 = 2.0$ m s^{-1}, $Re = 5200$, $We = 142$, and the target diameter is $D_s = 6$ mm. The predicted curves are computed using (3.21) with $\tau = 0.1$, $\eta = 0.38$. The impact angle is (*a*) $\alpha_i = 6.5^\circ$ and (*b*) $\alpha_i = 22^\circ$.

reformulated in the spherical coordinate system:

$$h_0^*(\theta_0) = \frac{\eta}{\tau^2} \exp\left[-\frac{6\eta\theta_0^2 k^2}{4\tau^2}\right]. \tag{3.25}$$

This approximate solution is valid if the thickness of the film is much smaller than the sphere radius. The theory correctly predicts the elevation of the film thickness with the angle α. The agreement between the theoretical predictions and the experiments is rather good, which means that the theory accounts for the main physical effects.

The parameters $\tau = 0.1$, $\eta = 0.38$, used for the calculation of both cases, are obtained by fitting the theory with the experimental data for time $t^* \approx 1$. It is obvious that these values should depend on the diameter ratios of the drop and target. The values of τ and η obtained by fitting the experimental data for various drop and target diameters are shown in figure 12.

It is important to note that this inviscid solution is valid only for cases when the viscous effects are negligibly small. At larger times, when the lamella thickness and the thickness of the viscous boundary layer are comparable, the viscous effects have to be taken into

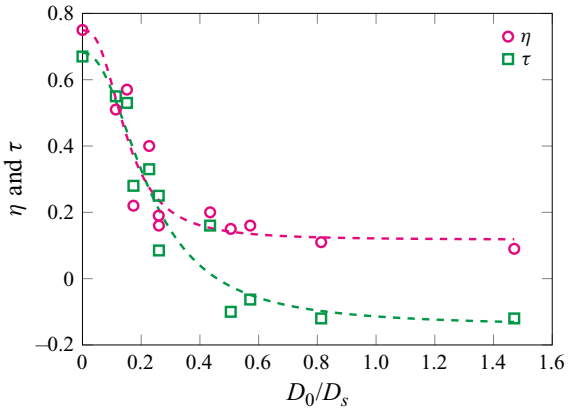

Figure 12. Estimated values of the dimensionless parameters τ and η obtained by fitting the measured evolution of the lamella height at $\alpha = \alpha_i$ using the theoretically predicted expression $h_i^* = \eta(t^* + \tau)^{-2}$ for various values of the ratio D_0/D_s.

account even for high Reynolds numbers. The effect of viscosity on the drop spreading will be considered in the next section.

4. Axisymmetric impact of a viscous drop

4.1. *Evolution of the lamella thickness*

In the axisymmetric cases, the inviscid solution (3.21) can be simplified, accounting for $\chi = 0$:

$$h^*_{inv} = h^*_0 \left(\frac{\theta\tau}{t^* + \tau}\right) \frac{\theta}{\sin\theta} \frac{\tau^2}{(t^* + \tau)^2}, \tag{4.1}$$

$$\alpha = \pm\theta. \tag{4.2}$$

Here and later in the text, the term h_{inv} is associated with the inviscid approximation of the flow.

Spreading of a drop on a solid substrate at $Re \gg 1$ is accompanied by an expansion of a viscous boundary layer of thickness $h_\nu \sim \sqrt{\nu t}$. It can be written in the dimensionless form $h^*_\nu \sim \sqrt{t^*}\, Re^{-1/2}$. The flow velocity slows down near the wall, leading to the generation of the normal component of the velocity. This flow has been analysed in the exact solution (Roisman 2009) for drop impact onto a dry, solid, planar substrate. This solution can be applied to the flow on a sphere if $h \ll R_s$:

$$h^* \approx h^*_{inv} + a\sqrt{t}\, Re^{-1/2}, \tag{4.3}$$

where $a \approx 0.48$ for a planar substrate. This value is applicable to the case of a spherical drop if the boundary layer thickness is much smaller than the sphere radius.

At some instant t_ν, the thickness of the boundary layer is equal to the lamella thickness. Its expression can be obtained using (4.1) and (4.3), leading to

$$t^*_\nu \sim \left[\frac{\theta}{\sin\theta}\right]^{2/5} Re^{1/5}. \tag{4.4}$$

At times $t > t_\nu$, the flow in the lamella is driven by the viscous stresses. The residual film thickness is obtained substituting the expression (4.4) for the time t_ν in (4.3), which

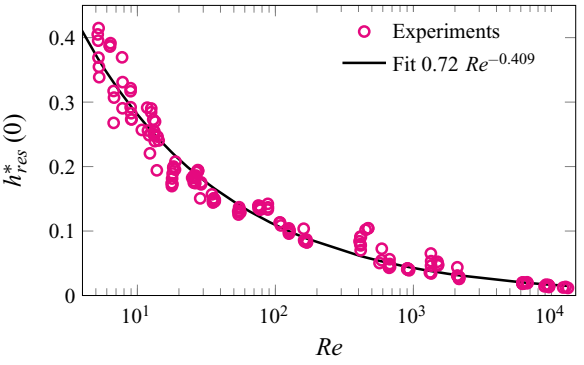

Figure 13. Non-dimensional residual thickness $h^*_{res}(0)$ at the sphere tip as a function of Re for the experiments with $9.91 < k < 19.32$. All individual experiments are plotted. The error in each experiment is less than 50 µm.

leads to

$$h^*_{res}(\theta) = A(k)\, Re^{-2/5} \left[\frac{\theta}{\sin\theta}\right]^{1/5}, \quad D_0 = 2R_0, \tag{4.5a,b}$$

where $A(k)$ is a dimensionless parameter determined by the geometry of impact, namely by the ratio $k = R_s/R_0$.

The results of measurements of the residual film thickness at the sphere tip for the cases $k \gg 1$ are shown in figure 13. The best fit of the data is obtained as

$$h^*_{res}(0) \approx 0.72\, Re^{-0.409}, \quad \text{for } k \gg 1. \tag{4.6}$$

This result is in very good agreement with the theory presented in (4.5*a*,*b*). It should be noted that for many practical reasons – for example, in the aim of viscosity estimation using the measurements of $h^*_{res}(0)$ – it could be recommended to use an empirical correlation (4.6), which can be considered as a result of the instrument calibration.

The experimental data on $h^*_{res}(0)$ were used for solving the inverse problem, namely for measurements of the viscosities of the liquids used in this study with the help of (4.6). For the viscosity estimations, only the cases have been used for which a clear plateau in the residual film thickness was observed. Certainly, the cases leading to the drop splash or cases of low Reynolds numbers have been considered invalid for viscosity measurements.

Table 2 shows a comparison between the viscosities measured using drop impact on a spherical target method as compared to traditional rheometry and corrected for the same temperatures based on the formulas given by Cheng (2008) with the adjustments from Volk & Kähler (2018). The results agree with each other for most viscosity values, as well as with the values from the literature, demonstrating the applicability of the drop impact technique. Traditional rheometry has error approximately 1 %. Significant deviation is obtained for low viscosity, such as distilled water. The reason is a very thin residual film whose thickness is comparable with the pixel size of the camera. Additionally, higher errors are associated with higher offset, while more axisymmetric impacts yield more accurate results. The criterion for the results in table 2 is that all impacts have less than 1 % offset. The target sphere diameter D_s is 30 mm, which has the highest spreading, lowest residual thickness, and the best chance not to be affected by the rim formation that blocks the view. The calibration equation $h^* = 0.7379\, Re^{-0.422}$ is used for more accurate results for the range $10 < k < 11.4$.

Fluid	$\mu_{(rheometry)}$ (mPa s)	$\mu_{(drop\ impact)}$ (mPa s)	Error
Distilled water	0.9	0.9	−0.06
40 % glycerol solution	4.3	4.1	−0.05
60 % glycerol solution	13.9	14.3	+0.03
80 % glycerol solution	74.9	78.1	+0.04
90 % glycerol solution	263.4	247.3	−0.06
95 % glycerol solution	521.1	515.9	−0.01
Glycerol	1258.9	1165.5	−0.07

Table 2. Drop impact viscometry results as compared to traditional rheometry results. The temperature is $T = 22 \pm 1\,^{\circ}\mathrm{C}$. The error is calculated as error $= (\mu_{impact} - \mu_R)/\mu_R$.

It is important to note that the relevance of the drop impact viscometry (DIV) method is not in its accuracy but in its applicability to situations that are not measurable by existing methods. It excels in measuring the viscosity of non-Newtonian liquids at high shear rates, a regime inaccessible to traditional rheometry. While commercial rheometers typically reach 1000 Hz, DIV experiments can achieve shear rates exceeding 10^6 Hz, depending on the liquid and impact velocity. This capability makes DIV valuable in analysing industrial processes such as pesticide application, paint droplet behaviour, and fuel injection. Additionally, DIV's rapid measurement, where the impact occurs in milliseconds, is ideal for characterizing liquids with time-dependent properties, such as volatile paints, suspensions, and emulsions prone to evaporation at low temperatures. Finally, DIV requires only microlitre-sized drops, making it suitable for analysing rare or expensive liquids such as biological fluids (blood, tears or insulin) or even mercury solutions.

4.2. *Maximum drop spreading*

Denote $S = k\theta_{rim}$ as the arc length of the wetted spot of the sphere. Here, θ_{rim} is the polar angle corresponding to the position of the drop rim. The rim initially spreads. Then the value of θ_{rim} at some instant reaches a maximum. Finally, if the surface is hydrophobic, then the rim can start to recede. The value of θ_{max} is an important parameter characterizing the level of the particle encapsulation after drop impact. It is determined mainly by the impact parameters, drop and sphere diameters, impact velocity, and liquid properties, including viscosity and surface tension.

In the case of drop impact onto a flat substrate, the expression for the maximum spreading diameter is obtained in Roisman (2009) from the analysis of the drop spreading on a plane accounting for the dynamics of the rim (1.2). The same ideas as in Roisman (2009) will be used in this study also for the description of the maximum spreading on a sphere. Let us assume first that the effects of surface tension can be neglected. Following (1.2), the volume of the rim can be neglected in comparison to the initial volume of the drop if $We^{1/2}/Re^{1/5} \gg 1$ and thus the second term on the right-hand side of (1.2) can be neglected in comparison with the first term.

The mass balance of the total volume of the residual lamella yields

$$\frac{\pi k^2}{2}\int_0^{\theta_v} h^*_{res}\sin\theta\,\mathrm{d}\theta = \frac{\pi}{6}, \tag{4.7}$$

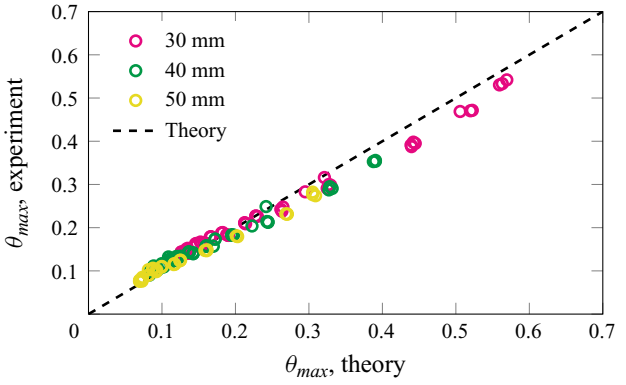

Figure 14. Comparison of the measured values for the maximum spreading angle θ_{max} with the theoretical predictions (4.10). The dashed line corresponds to perfect agreement. All individual experiments are plotted.

which can be simplified with the help of (4.5*a*,*b*) as

$$\int_0^{\theta_v} \theta^{1/5} \sin^{4/5}\theta \, \mathrm{d}\theta = \frac{Re^{2/5}}{3Ak^2}, \tag{4.8}$$

where θ_v is the approximate value of the maximum spreading angle if the effects of surface tension are neglected.

This equation does not have an exact solution. An approximate expression for the root of this equation, θ_v, valid in the range $\theta \in [0, \pi]$, is obtained after series expansions around $\theta = 0$ of the integrand on the left-hand side of (4.8) with precision θ^6:

$$\theta_v \approx \sqrt{15}\sqrt{1 - \left(1 - \frac{2\,Re^{2/5}}{15Ak^2}\right)^{1/3}}, \quad \text{if } We^{1/2}/Re^{1/5} \gg 1. \tag{4.9}$$

The expression for θ_v can be represented as an upper bound for the value θ_{max} since the considerations leading to (4.9) do not take into account the dynamics of the rim. The known characteristic rim velocity $u^*_{rim} \sim We^{-1/2}\,(h^*_{res})^{-1/2}$, the Taylor rim velocity (Taylor 1959; Roisman *et al.* 2002), is determined by the balance of inertial and interfacial forces applied to the rim. The corrected increment of the dimensionless spreading factor due to the rim motion is $\Delta S^* \sim t^*_v u^*_{rim}$. The final expression for the maximum spreading angle on a sphere $\theta_{max} = \theta_v - \Delta S^*/k$ is obtained with the help of (4.4), (4.5*a*,*b*) and (4.9) in the form

$$\theta_{max} = \sqrt{15}\sqrt{1 - \left(1 - \frac{2\,Re^{2/5}}{15Ak^2}\right)^{1/3}} - \frac{B\,Re^{2/5}}{k\,We^{1/2}\,A^{1/2}}\left[\frac{\theta_v}{\sin\theta_v}\right]^{3/10}, \tag{4.10}$$

where B is a fitting parameter.

It can be shown that the linearization of (4.10) for small values of $\theta_v \ll 1$, associated with an impact onto a flat substrate, leads to its reduction to the form (1.2). Moreover, noting that (1.2) is obtained in (Roisman 2009) for the value $A = 0.79$, the parameter $B \approx 0.36$ can be estimated. The measured values for the maximum spreading angle θ_{max} are in good agreement with the theoretical predictions of (4.10), as shown in figure 14.

The model is applicable only to the cases where the sphere is not completely encapsulated, namely when $\theta_v < \pi$. This condition, analysed with the help of (4.9), is

satisfied if

$$Re < 154.0\,A^{5/2}k^5. \tag{4.11}$$

The Reynolds number determined on the right-hand side of (4.11) is the threshold value for the complete sphere encapsulation.

For large values of k, the value of the parameter A approaches a constant corresponding to a flat target. If $\theta_v < 1$, then the term $(\theta_v/\sin\theta_v)^{3/10}$ is very close to unity. In this case, the expression (4.10) for θ_{max} can be further simplified to

$$\theta_{max} = \sqrt{15}\sqrt{1 - \left(1 - \frac{2\,Re^{2/5}}{15Ak^2}\right)^{1/3}} - \frac{0.40\,Re^{2/5}}{k\,We^{1/2}}. \tag{4.12}$$

It should be noted that some advanced theory for the lamella spreading and rim dynamics on a flat solid substrate has been developed recently by Gordillo, Riboux & Quintero (2019). It could be interesting to examine how this theory works in the case of not axisymmetric impact onto a curved surface. However, this topic is out of the framework of this study. Nevertheless, the current estimation of the maximum spreading on a spherical surface is sufficient to estimate the validity limits for the rheological measurements by drop impact, considered in this study.

5. Conclusion

In this study, the non-axisymmetric impact of a liquid viscous drop onto a solid, fixed spherical target is observed and characterized using a high-speed video system. Image processing allows us to measure the evolution of the lamella thickness in time and over the sphere surface. Observing the lamella thickness on a convex spherical surface becomes possible since it is not obscured by a rim formed at the edge of the spreading lamella.

In the theoretical part of the study, the inviscid solution and the viscous solution, developed previously for a drop impact onto a planar substrate, are generalized for the curved geometry of a spherical target. The theoretically predicted evolution of the drop shape, the profile of the residual film, and the spreading factor of the drop agree well with the experiments, which indicates that the main physical mechanisms are taken into account in the model.

Moreover, we introduce a novel method, drop impact viscometry, for *in situ* measurement of liquid viscosity at high shear rates through a single drop impact experiment. This technique holds promise for various industries reliant on non-Newtonian drops, such as pesticide spraying, paint droplet spreading, blood impact analysis, and fuel injection. Additionally, the experimental set-up facilitates rapid viscosity measurements, making it particularly valuable for liquids with quickly changing properties or limited availability.

Nomenclature

We	Weber number
Re	Reynolds number
Fr	Froude number
ρ	density
σ	surface tension
μ	dynamic viscosity
ν	kinematic viscosity

U_0	initial impact velocity
U_n	normal velocity component
U_τ	velocity component parallel to the target
D_0	initial drop diameter
D^*	spreading factor
D^*_{max}	maximum spreading factor
D_s	target diameter
R_s	target radius
R_0	initial drop radius
k	target to drop ratio
b	off-axis distance
α_i	off-axis angle
α_0	initial off-axis angle
g	gravitational constant (9.81 m s^{-2})
h_{res}	residual lamella thickness
h_v	viscous boundary layer thickness
h_i	lamella thickness at impact point α_i
r	radial coordinate
θ	polar angle
φ	azimuthal angle
u_θ	average velocity component in θ-direction
u_φ	average velocity component in φ-direction
p	pressure in the lamella
n	unit vector
$\kappa, \Omega, \tau, \chi, \eta, a, A, B$	dimensionless constants
T	temperature
S	arc length of the wetted spot
θ_v	maximum spreading angle if the effects of surface tension are neglected
θ_{max}	maximum spreading angle

Funding. This project has received funding from the European Union's Horizon 2020 research and innovation programme under the Marie Skłodowska-Curie grant agreement no. 955612 (NanoPaInt).

Declaration of interests. The authors report no conflict of interest.

Author ORCIDs.
Mete Abbot https://orcid.org/0000-0002-6077-8231;
Max Lannert https://orcid.org/0009-0006-9567-4471;
Awadhesh Kiran https://orcid.org/0000-0002-4897-9188;
Shamit Bakshi https://orcid.org/0000-0002-2073-9318;
Jeanette Hussong https://orcid.org/0000-0001-5152-1904;
Ilia V. Roisman https://orcid.org/0000-0002-9878-3650.

References

Aksoy, Y.T., Eneren, P., Koos, E. & Vetrano, M.R. 2022 Spreading of a droplet impacting on a smooth flat surface: how liquid viscosity influences the maximum spreading time and spreading ratio. *Phys. Fluids* **34** (4), 042106.

Bakshi, S., Roisman, I.V. & Tropea, C. 2007 Investigations on the impact of a drop onto a small spherical target. *Phys. Fluids* **19** (3), 032102.

BANITABAEI, S.A. & AMIRFAZLI, A. 2017 Droplet impact onto a solid sphere: effect of wettability and impact velocity. *Phys. Fluids* **29** (6), 062111.

BANITABAEI, S.A. & AMIRFAZLI, A. 2020 Droplet impact onto a solid sphere in mid-air: effect of viscosity, gas density, and diameter ratio on impact outcomes. *Phys. Fluids* **32** (3), 037102.

BERBEROVIĆ, E., VAN HINSBERG, N.P., JAKIRLIĆ, S., ROISMAN, I.V. & TROPEA, C. 2009 Drop impact onto a liquid layer of finite thickness: dynamics of the cavity evolution. *Phys. Rev.* E **79** (3), 036306.

BISIGHINI, A., COSSALI, G.E., TROPEA, C. & ROISMAN, I.V. 2010 Crater evolution after the impact of a drop onto a semi-infinite liquid target. *Phys. Rev.* E **82** (3), 036319.

BORDBAR, A., TAASSOB, A., KHOJASTEH, D., MARENGO, M. & KAMALI, R. 2018 Maximum spreading and rebound of a droplet impacting onto a spherical surface at low Weber numbers. *Langmuir* **34** (17), 5149–5158.

CHARALAMPOUS, G. & HARDALUPAS, Y. 2017 Collisions of droplets on spherical particles. *Phys. Fluids* **29** (10), 103305.

CHENG, L. 1977 Dynamic spreading of drops impacting onto a solid surface. *Ind. Engng Chem. Proc. DD* **16** (2), 192–197.

CHENG, N.-S. 2008 Formula for the viscosity of a glycerol–water mixture. *Ind. Engng Chem. Res.* **47** (9), 3285–3288.

CHENG, X., SUN, T.-P. & GORDILLO, L. 2022 Drop impact dynamics: impact force and stress distributions. *Annu. Rev. Fluid Mech.* **54**, 57–81.

COSSALI, G.E., COGHE, A.L.D.O. & MARENGO, M. 1997 The impact of a single drop on a wetted solid surface. *Exp. Fluids* **22** (6), 463–472.

DALGAMONI, H.N. & YONG, X. 2021 Numerical and theoretical modeling of droplet impact on spherical surfaces. *Phys. Fluids* **33** (5), 052112.

DU, J., WANG, X., LI, Y., MIN, Q. & WU, X. 2021 Analytical consideration for the maximum spreading factor of liquid droplet impact on a smooth solid surface. *Langmuir* **37** (24), 7582–7590.

FAN, Z., LIU, D., PAN, S., MA, J. & CHEN, X. 2023 Spreading dynamics of the viscous droplet impacting on a spherical particle. *Phys. Fluids* **35** (2), 023311.

FUDGE, B.D., CIMPEANU, R., ANTKOWIAK, A., CASTREJÓN-PITA, J.R. & CASTREJÓN-PITA, A.A. 2023 Drop splashing after impact onto immiscible pools of different viscosities. *J. Colloid Interface Sci.* **641**, 585–594.

GAO, X. & LI, R. 2014 Spread and recoiling of liquid droplets impacting solid surfaces. *AIChE J.* **60** (7), 2683–2691.

GORDILLO, J.M., RIBOUX, G. & QUINTERO, E.S. 2019 A theory on the spreading of impacting droplets. *J. Fluid Mech.* **866**, 298–315.

HARDALUPAS, Y., TAYLOR, A.M.K.P. & WILKINS, J.H. 1999 Experimental investigation of sub-millimetre droplet impingement on to spherical surfaces. *Intl J. Heat Fluid Flow* **20** (5), 477–485.

HOWLAND, C.J., ANTKOWIAK, A., CASTREJÓN-PITA, J.R., HOWISON, S.D., OLIVER, J.M., Style, R.W. & Castrejón-Pita, A.A. 2016 It's harder to splash on soft solids. *Phys. Rev. Lett.* **117** (18), 184502.

JAISWAL, A.K. & KHANDEKAR, S. 2021 Drop-on-drop impact dynamics on a superhydrophobic surface. *Langmuir* **37** (43), 12629–12642.

JOSSERAND, C. & THORODDSEN, S.T. 2016 Drop impact on a solid surface. *Annu. Rev. Fluid Mech.* **48**, 365–391.

KHURANA, G., SAHOO, N. & DHAR, P. 2019 Phenomenology of droplet collision hydrodynamics on wetting and non-wetting spheres. *Phys. Fluids* **31** (7), 072003.

KITTEL, H.M., ROISMAN, I.V. & TROPEA, C. 2018 Splash of a drop impacting onto a solid substrate wetted by a thin film of another liquid. *Phys. Rev. Fluids* **3** (7), 073601.

LEMBACH, A.N., TAN, H.-B., ROISMAN, I.V., GAMBARYAN-ROISMAN, T., ZHANG, Y., TROPEA, C. & YARIN, A.L. 2010 Drop impact, spreading, splashing, and penetration into electrospun nanofiber mats. *Langmuir* **26** (12), 9516–9523.

LIU, X., ZHANG, X. & MIN, J. 2019 Maximum spreading of droplets impacting spherical surfaces. *Phys. Fluids* **31** (9), 092102.

LUO, J., CHU, F., NI, Z., ZHANG, J. & WEN, D. 2021 Dynamics of droplet impacting on a cone. *Phys. Fluids* **33** (11), 112116.

MAO, T., KUHN, D.C.S. & TRAN, H. 1997 Spread and rebound of liquid droplets upon impact on flat surfaces. *AIChE J.* **43** (9), 2169–2179.

MARENGO, M., ANTONINI, C., ROISMAN, I.V. & TROPEA, C. 2011 Drop collisions with simple and complex surfaces. *Curr. Opin. Colloid Interface Sci.* **16** (4), 292–302.

MARMANIS, H. & THORODDSEN, S.T. 1996 Scaling of the fingering pattern of an impacting drop. *Phys. Fluids* **8** (6), 1344–1346.

MITRA, S., EVANS, G.M., DOROODCHI, E., PAREEK, V. & JOSHI, J.B. 2017 Interactions in droplet and particle system of near unity size ratio. *Chem. Engng Sci.* **170**, 154–175.

MITRA, S., NGUYEN, T.B.T., DOROODCHI, E., PAREEK, V., JOSHI, J.B. & EVANS, G.M. 2016 On wetting characteristics of droplet on a spherical particle in film boiling regime. *Chem. Engng Sci.* **149**, 181–203.

MITRA, S., SATHE, M.J., DORRODCHI, E., PAREEK, V., JOSHI, J.B. & EVANS, G. 2013 In-flight collision behaviour of droplets on a spherical particle falling under gravity. In *Proceedings of 8th World Conference on Experimental Heat Transfer, Fluid Mechanics, and Thermodynamics, Lisbon, Portugal* (ed. P.J. Coelho & M. Costa). Instituto Superior Técnico (IST).

MOCK, U., MICHEL, T., TROPEA, C., ROISMAN, I. & RÜHE, J. 2005 Drop impact on chemically structured arrays. *J. Phys.: Condens. Matter* **17** (9), S595.

PASANDIDEH-FARD, M., QIAO, Y.M., CHANDRA, S. & MOSTAGHIMI, J. 1996 Capillary effects during droplet impact on a solid surface. *Phys. Fluids* **8** (3), 650–659.

PAWAR, S.K., HENRIKSON, F., FINOTELLO, G., PADDING, J.T., DEEN, N.G., JONGSMA, A., INNINGS, F. & KUIPERS, J.A.M.H. 2016 An experimental study of droplet–particle collisions. *Powder Technol.* **300**, 157–163.

POU, P., DEL VAL, J., RIVEIRO, A., COMESAÑA, R., ARIAS-GONZÁLEZ, F., LUSQUIÑOS, F., BOUNTINGUIZA, M., QUINTERO, F. & POU, J. 2019 Laser texturing of stainless steel under different processing atmospheres: from superhydrophilic to superhydrophobic surfaces. *Appl. Surf. Sci.* **475**, 896–905.

RIBOUX, G. & GORDILLO, J.M. 2014 Experiments of drops impacting a smooth solid surface: a model of the critical impact speed for drop splashing. *Phys. Rev. Lett.* **113** (2), 024507.

RIOBOO, R., MARENGO, M. & TROPEA, C. 2002 Time evolution of liquid drop impact onto solid, dry surfaces. *Exp. Fluids* **33** (1), 112–124.

RIOBOO, R., TROPEA, C. & MARENGO, M. 2001 Outcomes from a drop impact on solid surfaces. *Atomiz. Sprays* **11** (2), 155–165.

ROISMAN, I.V. 2009 Inertia dominated drop collisions. II. An analytical solution of the Navier–Stokes equations for a spreading viscous film. *Phys. Fluids* **21** (5), 052103.

ROISMAN, I.V. 2010 Fast forced liquid film spreading on a substrate: flow, heat transfer and phase transition. *J. Fluid Mech.* **656**, 189–204.

ROISMAN, I.V., BERBEROVIĆ, E. & TROPEA, C. 2009 Inertia dominated drop collisions. I. On the universal flow in the lamella. *Phys. Fluids* **21** (5), 052103.

ROISMAN, I.V., LEMBACH, A. & TROPEA, C. 2015 Drop splashing induced by target roughness and porosity: the size plays no role. *Adv. Colloid Interface Sci.* **222**, 615–621.

ROISMAN, I.V., RIOBOO, R. & TROPEA, C. 2002 Normal impact of a liquid drop on a dry surface: model for spreading and receding. *Proc. R. Soc. Lond.* A **458** (2022), 1411–1430.

SCHELLER, B.L. & BOUSFIELD, D.W. 1995 Newtonian drop impact with a solid surface. *AIChE J.* **41** (6), 1357–1367.

SECHENYH, V. & AMIRFAZLI, A. 2016 An experimental study for impact of a drop onto a particle in mid-air: the influence of particle wettability. *J. Fluids Struct.* **66**, 282–292.

STUMPF, B., HUSSONG, J. & ROISMAN, I.V. 2022 Drop impact onto a substrate wetted by another liquid: flow in the wall film. *Colloid Interface* **6** (4), 58.

SYKES, T.C., FUDGE, B.D., QUETZERI-SANTIAGO, M.A., CASTREJÓN-PITA, J.R. & Castrejón-Pita, A.A. 2022 Droplet splashing on curved substrates. *J. Colloid Interface Sci.* **615**, 227–235.

TANG, C., QIN, M., WENG, X., ZHANG, X., ZHANG, P., LI, J. & HUANG, Z. 2017 Dynamics of droplet impact on solid surface with different roughness. *Intl J. Multiphase Flow* **96**, 56–69.

TAYLOR, G.I. 1959 The dynamics of thin sheets of fluid II. Waves on fluid sheets. *Proc. R. Soc. Lond.* A **253** (1274), 296–312.

UKIWE, C. & KWOK, D.Y. 2005 On the maximum spreading diameter of impacting droplets on well-prepared solid surfaces. *Langmuir* **21** (2), 666–673.

VOLK, A. & KÄHLER, C.J. 2018 Density model for aqueous glycerol solutions. *Exp. Fluids* **59** (5), 75.

WILDEMAN, S., VISSER, C.W., SUN, C. & LOHSE, D. 2016 On the spreading of impacting drops. *J. Fluid Mech.* **805**, 636–655.

WORTHINGTON, A.M. 1876 On the form assumed by drops of liquids falling vertically on a horizontal plate. *Proc. R. Soc. Lond.* A **25**, 261–271.

YAN-PENG, L. & HUAN-RAN, W. 2011 Three-dimensional direct simulation of a droplet impacting onto a solid sphere with low-impact energy. *Can. J. Chem. Engng* **89** (1), 83–91.

YARIN, A.L. 2006 Drop impact dynamics: splashing, spreading, receding, bouncing …. *Annu. Rev. Fluid Mech.* **38**, 159–192.

YARIN, A.L., ROISMAN, I.V. & TROPEA, C. 2017 *Collision Phenomena in Liquids and Solids*. Cambridge University Press.

YARIN, A.L. & WEISS, D.A. 1995 Impact of drops on solid surfaces: self-similar capillary waves, and splashing as a new type of kinematic discontinuity. *J. Fluid Mech.* **283**, 141–173.

YOON, I. & SHIN, S. 2021 Maximal spreading of droplet during collision on particle: effects of liquid viscosity and surface curvature. *Phys. Fluids* **33** (8), 083310.

ZHANG, D., PAPADIKIS, K. & GU, S. 2014 Application of a high density ratio lattice-Boltzmann model for the droplet impingement on flat and spherical surfaces. *Intl J. Therm. Sci.* **84**, 75–85.

ZHANG, X., JIAN, Z., HOU, B. & THORAVAL, M.-J. 2022 Drop impact on a sessile soap bubble. *Phys. Fluids* **34** (12), 122116.

ZHU, Y., LIU, H.-R., MU, K., GAO, P., DING, H. & LU, X.-Y. 2017 Dynamics of drop impact onto a solid sphere: spreading and retraction. *J. Fluid Mech.* **824**, R3.